Supplementary Information

A Effect of the penalisation exponent p

In this paper a value of $p = 2$ for the penalisation factor has been used throughout. This choice of p came as a result of test simulations with different values of p. Optimal structures at step 100 for the p values of 1, 2, and 3 are shown in Fig. 15.

The $p = 1$ case leads to a structure with a large fraction of "gray" particles, featuring intermediate χ between 0 and 1. This result is similar to what may be obtained in variable thickness sheet problems [58], but it is not a desirable outcome for the type of optimization problems studied here, where the final result should be as close as possible to a 0–1, void–solid solution only. $p = 2$ and $p = 3$ both lead to black and white solutions. The structure obtained with $p = 3$ has a more complex topology, featuring more elements, which might make it more difficult to fabricate. This greater complexity may come from the tendency of optimization problems with high penalization levels, i.e. high p, to get trapped into local minima of the objective function; such tendency is known in the literature on FEM-based TO [54].

The speed of convergence, for the three cases with different p, is show in Fig. 16. All three cases eventually converge to a similar value of the objective function, meaning that the choice of p for the problems in this manuscript is not driven by the ability to better minimize the objective function. To compare the speed of convergence, we fitted the curves in Fig. 16 using an exponential function of the type $f(x) = k_1 + k_2 e^{\frac{n}{k_3}}$, where n is the step number during the optimization process.

Table 2 shows the fitted values for k_1, k_2 and k_3. Among those, k_1 controls the final value of the objective function, hence it is similar for the three cases of p shown here. k_2, summed to k_1, gives the starting value of the objective function at step 1, so it correctly increases with p, as the initial structures with all particles featuring χ between 0 and 1 are less stiff when subjected to a high penalization factor. k_3 controls the speed of convergence: the higher k_3, the slower the convergence, i.e. more optimization steps are required to attain the final value of the objective function. The values of k_3 in Table 2 are quite similar for the three cases of p considered here, with $p = 2$ being a bit slower.

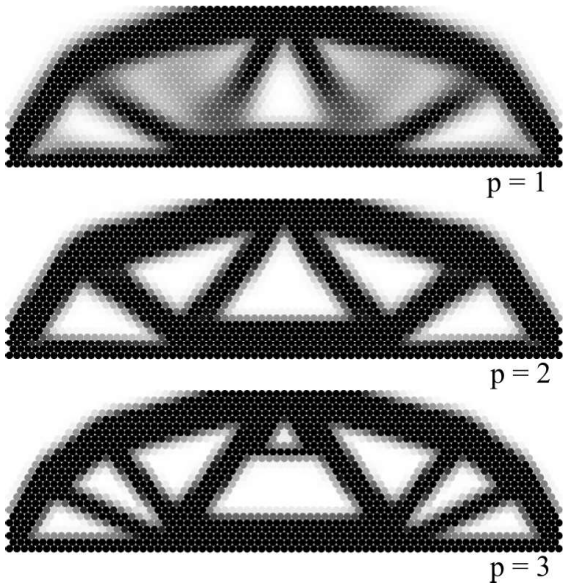

Fig. 15 Optimization of a beam domain, made of 75 × 25 particles, with D = 1 and filtering of 1.1 applied, simply supported beam at the bottom left and right ends. Three values of penalization factors p are investigated. The snapshot show the solutions at optimization step 100.

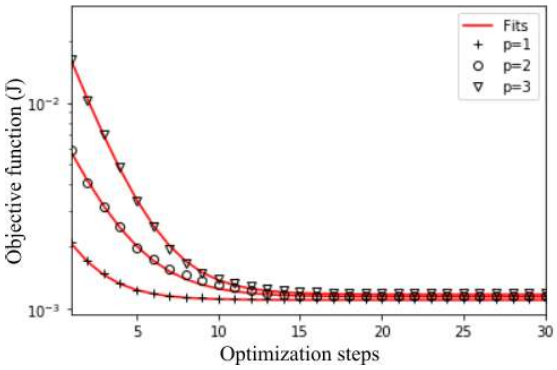

Fig. 16 Convergence of the optimization problems in Fig. 15. The fits are obtained using the exponential function discussed in the main body of the text.

p	k_1 (J)	k_2 (J)	k_3
1	0.0011	0.0016	2.0
2	0.00114	0.007	2.4
3	0.00117	0.025	2.1

Table 2 Constants used for the fits in Fig. 16

All in all, the results in this section led us to avoid $p = 1$, as it generates undesirably gray structures. Our preference for

$p = 2$ over $p = 3$ stemmed from the lower topological complexity of the solutions obtained with $p = 2$, despite this required a few more optimization steps to achieve convergence. Furthermore, we considered $p = 2$ more recommendable also for future, different studies, knowing from FE-based TO that problems with high p tend to get trapped into local minima.

B Perturbation method to compute full sensitivities

In the main manuscript, we discussed how the sensitivity expression in Eq. 13 is an approximation of the gradient of the cost function with respect to the design variables. Here we present a numerical perturbation method for computing the full sensitivity and then we compare optimization results from this perturbation method with results obtained using the approximate sensitivity in Eq. 13.

The full sensitivity vector is computed one term at the time. At the generic step of the optimization process, the structure displays a certain vector of χ_i values, and a complementary work U^*_{eq} at equilibrium under the imposed external forces. The generic term $\frac{dc}{d\chi_i}$ of the sensitivity vector is obtained perturbing the value of χ_i by a small quantity $\Delta\chi$ and computing the new value of U^* resulting from a new energy minimization. The sensitivity is thus approximated by finite difference as:

$$\frac{dc}{d\chi_i} \approx \frac{\Delta U^*}{\Delta\chi_i} = \frac{U^*(\chi_i + \Delta\chi_i) - U^*_{eq}(\chi_i)}{\Delta\chi_i} \tag{22}$$

This is repeated for all particles i in the structure. This procedure has a high computational cost, in that each term of the sensitivity vector requires one dedicated energy minimization to compute the perturbed U^*. Therefore here we consider only small structures, made of 45×15 particles, to compare results from this numerical approach and the approximated sensitivity used in the main manuscript (Eq. 13). The geometry, supports, and loading conditions are the same as for the double-pinned, central force beams in Fig. 14.e in the main manuscript. The systems are loaded with three force intensities, 0.2, 2, and 20 kN, to trigger different levels of geometric nonlinearity. Figs. 17, 18, and 19 show the results for these case studies, including results from both the numerical perturbation method (left) and the approximate sensitives (right). In these examples, the tolerance for DEM convergence has been set to 10^{-8}, the filtering length to 1.1 diameters, and the perturbation $\Delta\chi$ to 0.01.

All results in Figs. 17, 18, and 19 indicate that the two methods to compute sensitivities give results that are extremely similar, both in small and large deformation regimes (imposed by applying a progressively larger external load from one figure to the next). The figures also feature histograms showing the distribution of normalised per-particle i differences between the sensitivities obtained with the two methods:

$$E_i = \frac{\left| \left(\frac{dc}{d\chi_i}\right)_f - \left(\frac{\partial c}{\partial \chi_i}\right)_p \right|}{\frac{1}{N}\sum_i \left|\frac{dc}{d\chi_i}\right|_f} \tag{23}$$

In the equation, N is the number of particles in the domain. Subscripts f and p indicate *full* sensitivities computed using the numerical perturbation method presented here, and *partial* sensitivities obtained with the approximation in Eq. 13. Both the difference in the numerator and the contribution to the average in the denominator are taken as absolute values.

Fig. 20 shows that the particles with highest differences in sensitivity are those with intermediate χ between 0 and 1, mostly located at the boundaries between solid. Particles in the solid also display a certain level of difference in sensitivity, whereas void particles tend to zero sensitivity in both approaches as the optimization process converges. Consistently, the histograms in Figs. 17–19 start from a single peak distribution at step 1 towards bimodal distributions as the optimization progresses. In particular, a peak for differences tending to zero is formed and grows: this reflects the increase in void-like particles. The other peak in the histograms instead increases by approximately one order of magnitude, from differences of $0.001 - 0.01\%$ to $0.01 - 0.1\%$, during the first 15 steps of the optimization. This is when the structure gains most of its stiffness, thus reducing significantly the comple-

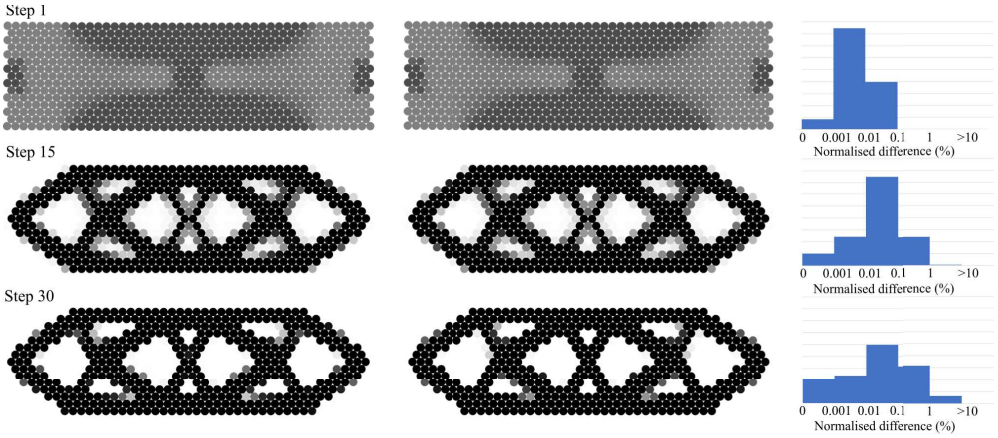

Fig. 17 Optimization of beam made of 45 × 15 particles, simply supported and loaded as shown in Fig. 13.a in the main manuscript. Here a load of 0.2 kN is applied, which leads to small deformations and an overall symmetric solution. Optimization snapshots at steps 1, 15, and 30 are shown, for full sensitivities (computed with the numerical perturbation method in this section) and for the approximate sensitivity in Eq. 13 (left and right columns respectively). For the same steps, the histograms quantify the difference between per-particle sensitivities obtained with the two methods (Eq. 23).

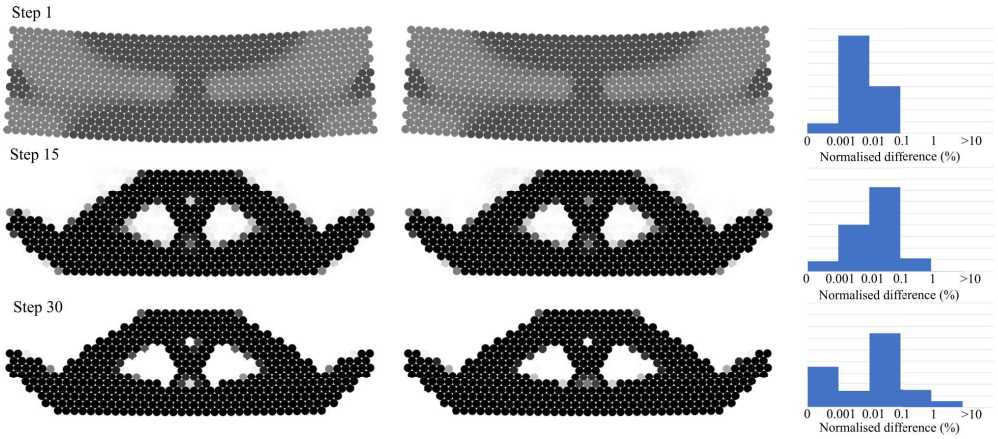

Fig. 18 Optimization of beam made of 45 × 15 particles, simply supported and loaded as shown in Fig. 13.a in the main manuscript. Here a load of 2 kN is applied, which is sufficient to highlight the effect of large deformations. Optimization snapshots at steps 1, 15, and 30 are shown, for full sensitivities (computed with the numerical perturbation method in this section) and for the approximate sensitivity in Eq. 13 (left and right columns respectively). For the same steps, the histograms quantify the difference between per-particle sensitivities obtained with the two methods (Eq. 23).

mentary energy and therefore the average magnitude of sensitivities in the structure, as shown in Fig. 21. As a result, the denominator in Eq. 23 decreases significantly during the first 15 optimization steps, and this shifts the normalised values in the histograms up. Comparing the histograms at step 15 with those at step 30, one can notice tail forming, with particles that feature high normalised differences up to 10%. These are the particles concentrating into a progressively thinner interface between solid and void. In any case, the histograms in the snapshots in Figs. 17–19 show that the differences between full and partial sensitivities are very small: fractions of percent. This is consistent with the fact that the optimum solutions, shown in the snapshots of the same figures, are nearly identical for the two methods of computing sensitivities.

In the main manuscript we discussed how the approximated sensitivity in Eq. 13 is actually exact in the limit of small strain, for linear elastic structures. By contrast, the cases with highest geometric nonlinearity are those where the differences between full and partial sensitivities might be most significant. However, the histograms in Figs. 17–19 indicate that the levels of nonlineariy explored here, while leading to qualitatively different structures, still imply a similar

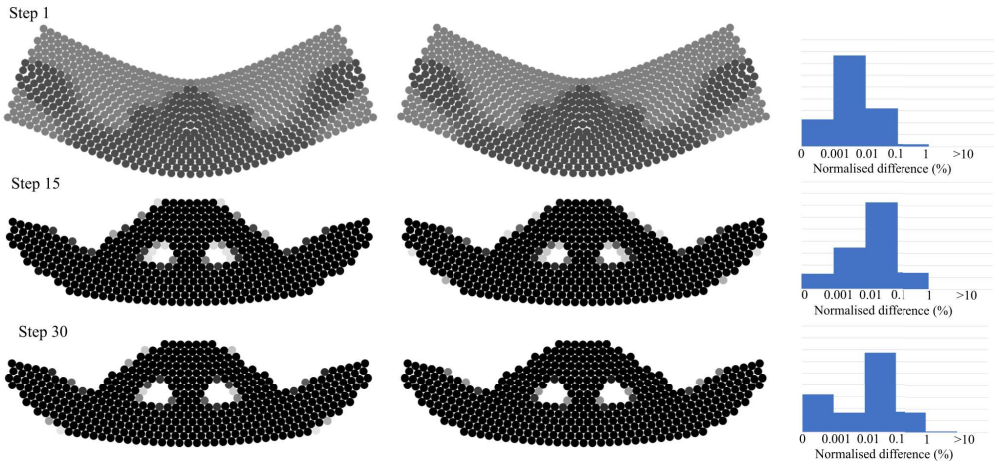

Fig. 19 Optimization of 45×15 beam, simply supported and loaded as shown in Fig. 13.a in the main manuscript. Here a high load of 20 kN is applied, which causes visibly large deformations. Optimization snapshots at steps 1, 15, and 30 are shown, for full sensitivities (computed with the numerical perturbation method in this section) and for the approximate sensitivity in Eq. 13 (left and right columns respectively). For the same steps, the histograms quantify the difference between per-particle sensitivities obtained with the two methods.

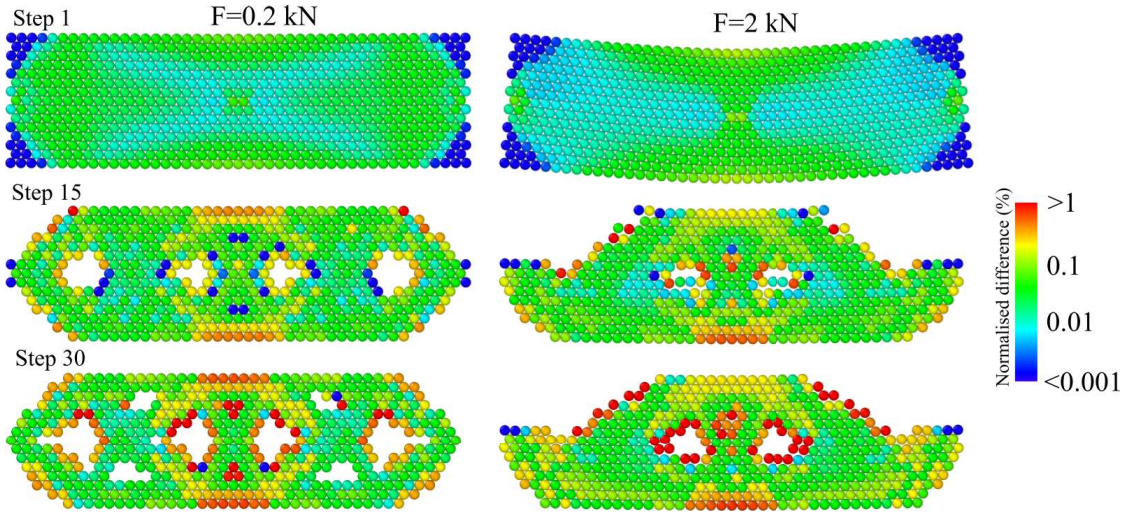

Fig. 20 Spatial distribution of normalised difference in sensitivity for the structures in Figs. 17 and 18(with 0.2 and 2 kN applied) showing the transition from an initially even spread of difference to concentrated error values in the solid-void border as the optimization progresses.

distribution of differences between full and partial sensitivities, i.e. the approximation in Eq. 13 seems quite robust to the geometric nonlinearity sampled here. The good quality of the approximation is indeed confirmed in Fig. 22, which shows the evolution of the objective function, i.e. the complementary work, during the optimization of the structure with highest load and thus highest geometric nonlinearity, from Fig. 19. The figure clearly indicates that, for the problems in this manuscript, the approximate sensitivity from Eq. 13 produces an optimization process that is quantitatively very similar to that obtained using the full sensitivity from the numerical perturbation method presented here.

C Unfiltered structure comparison

The main manuscript has shown that DEM-based TO using mesh-independent filtering leads to mesh-independent solutions, as expected. Here we consider the same structures as in Fig. 11 of the main manuscript, but now without filtering. Unfiltered simulations are in fact more likely to display mesh

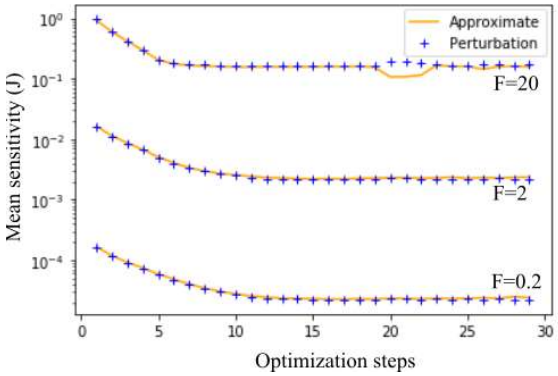

Fig. 21 Approximate and full mean sensitivity values during the first 30 steps of the optimization showing a fast decrease in all three cases.

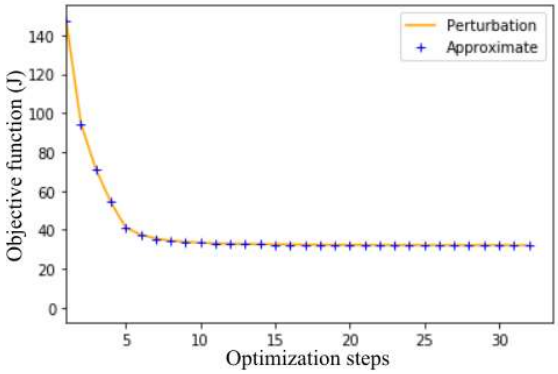

Fig. 22 Evolution of objective function (complementary work) for the problem in Fig. 19 (with 20 kN of applied load) solved using the full perturbation method and the approximate sensitivity in Eq. 13.

dependence. Fig. 23 shows results for 5 different meshes, including the base case used in the main manuscript. The same figure also includes results for similar meshes obtained using the FEM-based topology optimization code in Ref. [45]. Both the DETO and FEM-TO results show that the qualitative results is quite stable for all meshes from 75×25 and finer. Qualitative changes in the optimised topology emerge only in the coarsest cases. We consider this result appropriate for the type of structure and range of mesh fineness considered here: other structures, e.g. thinner beam domains, or even finer meshes may lead to more significant qualitative mesh effects. A more interesting result in Fig. 23 concerns instead the checkerboard problem, which clearly affects the FEM-TO solutions at any mesh whereas it is completely absent in all the solutions from DETO.

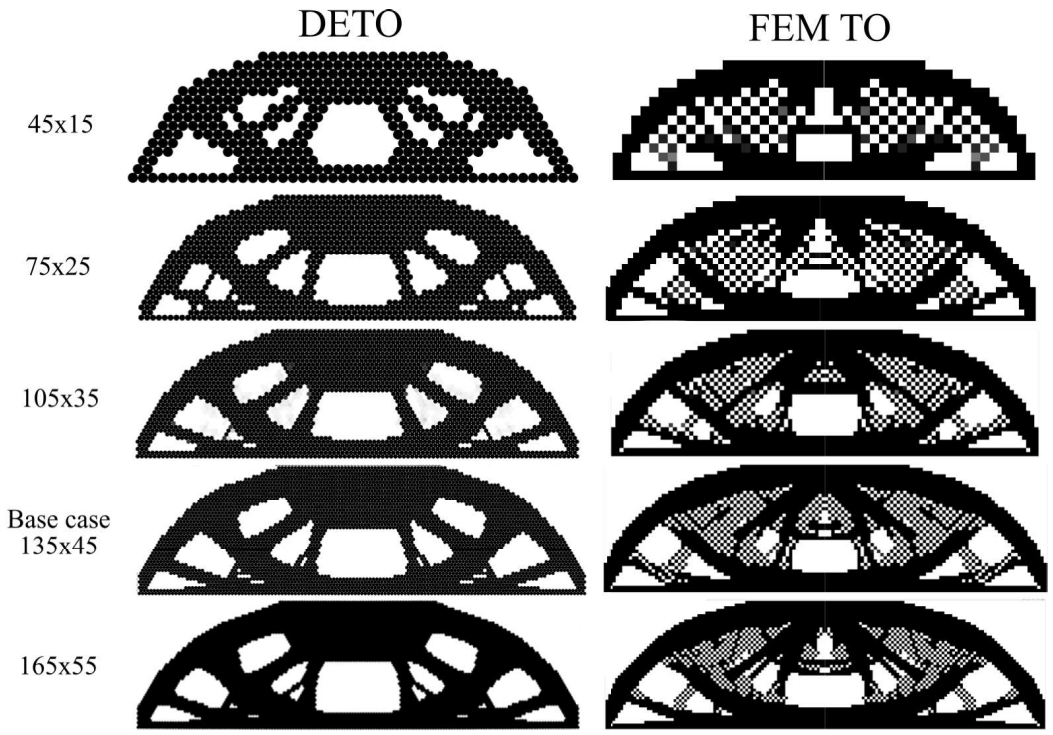

Fig. 23 Study on mesh effects for the same beam structures as in Fig. 23, but here without imposing any filtering. Results from our DE Topology Optimization method are compared to analogous results from the FEM-based optimization code in Ref. [45].